Exact diagonalization study of spin, orbital, and lattice correlations in CMR manganites

Alexander Weiße[1], Gerhard Wellein[2], and Holger Fehske[3,1]

[1] Physikalisches Institut, Universität Bayreuth, D-95440 Bayreuth
[2] Regionales Rechenzentrum Erlangen, Universität Erlangen, D-91058 Erlangen
[3] Institut für Physik, Universität Greifswald, D-17487 Greifswald

Abstract. To understand the interplay of spin, orbital and lattice degrees of freedom in colossal magneto-resistance manganites we numerically diagonalize an SU(2) symmetric spin-orbital model coupled to dynamic Jahn-Teller and Holstein-type phonons. For a four site cluster we demonstrate how the coupling to the lattice changes the order of spins, orbitals and charges, and the correlations between them.

1 Introduction

The transition from a metallic ferromagnetic low-temperature phase to an insulating paramagnetic high-temperature phase observed in some hole-doped manganese oxides (e.g. in $\mathrm{La_{1-x}[Sr,Ca]_xMnO_3}$) is associated with an unusual dramatic change in their electronic and magnetic properties, including a spectacularly large negative magneto-resistive response to an applied magnetic field, which might have important technological applications [1].

Apart from this so-called colossal magneto-resistance (CMR) transition hole-doped manganites exhibit a very complex and fascinating phase diagram (see Fig. 1). As a result of the subtle interplay of almost all degrees of freedom known in solid state physics different crystal structures and magnetic, charge and orbital ordered states are observed experimentally in dependence on temperature and doping level. Although such a striking behaviour has stimulated a considerable amount of both experimental and theoretical work [2] in the last decades, much of the basic physics of the CMR still remains controversial.

At present, there has been a renewed interest in simplified model Hamiltonians, capable of describing both the electronic structure of CMR manganites as well as the many-body correlations due to the interaction of charge, spin, orbital, and lattice degrees of freedom. Computational techniques then provide a useful tool to analyze the properties of these microscopic Hamiltonians, at least, in the difficult regime, where the correlations are strong and all interactions have to be treated on an equal footing. Within our HLRS project, reported on in this paper, we went a step in this direction by exactly diagonalizing a rather general low-energy model for the CMR manganites on a small cluster.

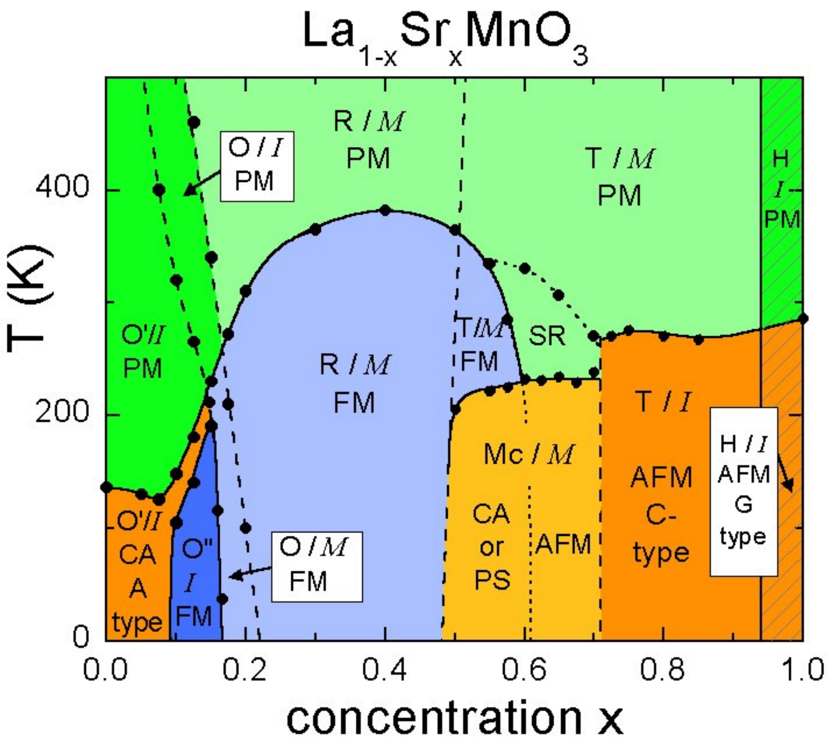

Fig. 1. Phase diagram of $La_{1-x}Sr_xMnO_3$ taken from Ref. [3]. The crystal structures (Jahn-Teller distorted orthorhombic: O', orthorhombic: O, orbital-ordered orthorhombic: O", rhombohedral: R, tetragonal: T, monoclinic: Mc, and hexagonal: H) are indicated as well as the magnetic structures (paramagnetic: PM (green), short-range order (SR), canted (CA), A-type antiferromagnetic structure: AFM (yellow); ferromagnetic: FM (blue), phase separated (PS), and AFM C-type structure) and the electronic state (insulating: I (dark); metallic: M (light)).

2 Theoretical model

The key elements of the electronic structure of the manganites are the partially filled 3d states. The cubic environment of the Mn sites within the perovskite lattice results in a crystal field splitting of Mn d-orbitals into e_g and t_{2g} (cf. Fig. 2). In the case of zero doping ($x = 0$) there are four electrons per Mn site which fill up the three t_{2g} levels and one e_g level, and by Hund's rule coupling (J_h), form a $S = 2$ spin state. Doping will remove the electron

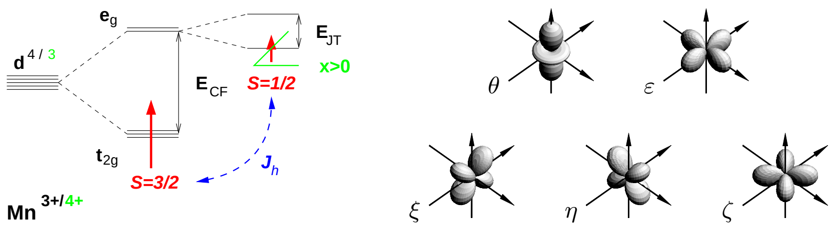

Fig. 2. Left: Crystal-field and Jahn-Teller splitting of the five-fold degenerate atomic Mn $3d$ levels (half-filled t_{2g} triplets form local spins $S = 3/2$ interacting ferromagnetically with electrons in single occupied e_g levels); right: e_g (θ, ε) and t_{2g} (ξ, η, ζ) orbitals.

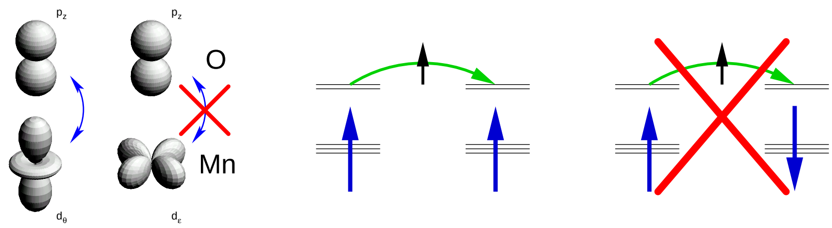

Fig. 3. Left: Along z-direction, electrons can hop only from $\theta = |3z^2 - r^2\rangle$ orbitals; transfer processes involving $\varepsilon = |x^2 - y^2\rangle$ orbitals are forbidden due to vanishing overlap with the in-between O $2p$ states. Right: Double-exchange model: If on-site Coulomb interaction U and Hund's coupling J_h are strong, hopping is allowed if the core spins are aligned and vanishes in the case of antiparallel orientation, i.e., itinerant e_g electrons cause a ferromagnetic interaction of localized t_{2g} spins.

from the e_g level, and by hopping via bridging oxygen sites the resulting holes acquire mobility.

Due to the specific symmetry of the manganese d and oxygen p orbitals, the transfer of the e_g-electrons shows a pronounced (orbital) anisotropy (see Fig. 3). In the limit of large on-site Coulomb interaction U and Hund's rule coupling J_h the electron transfer is strongly affected by the spin of the core electrons as well. Concentrating on the link between magnetic correlations and transport, early studies on lanthanum manganites attributed the low-T metallic behaviour to Zener's double-exchange mechanism, which maximizes the hopping of a strongly Hund's rule coupled e_g-electron in a polarized background of the Mn t_{2g}-electron spins (see Fig. 3).

Recently it has been realized that physics beyond double-exchange is important not only to explain the phase diagram of the manganites but also the CMR transition itself. In particular, orbital and lattice effects seem to be crucial in explaining the CMR phenomenon. More specifically, the orbital degeneracy in the ground state of Mn^{3+} ions connects the system to the lattice, making it sensible to Jahn-Teller distortion and polaronic effects.

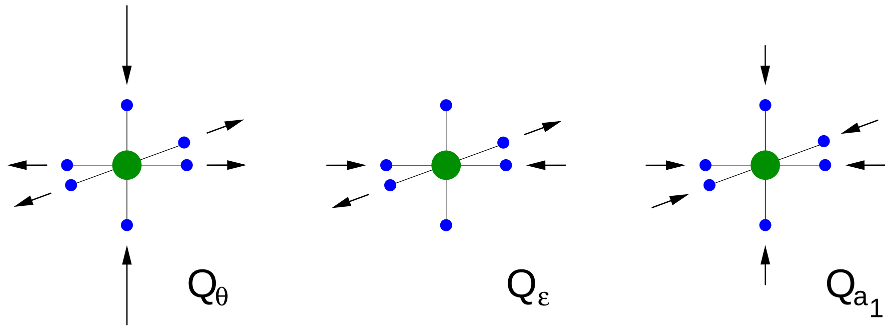

Fig. 4. Jahn-Teller and breathing-type phonon modes.

There are two types of lattice distortions which are important in manganites (see Fig. 4). First the partially filled e_g states of the Mn^{3+} ion are Jahn-Teller active, i.e., the system can gain energy from a quadrupolar symmetric elongation of the oxygen octahedra which lifts the e_g degeneracy. A second possible deformation is an isotropic shrinking of a MnO_6 octahedron. This "breathing"-type distortion couples to changes in the e_g charge density, i.e., is always associated with the presence of an Mn^{4+} ion. In the heavily doped material, both, breathing-mode collapsed (Mn^{4+}) and Jahn-Teller distorted (Mn^{3+}) sites are created simultaneously when the holes are localized in passing the CMR metal insulator transition.

Restricting the electronic Hilbert space to the large Hund's rule states given by the spin-2 orbital doublet state $^5E\ [t_2^3(^4A_2)e]$ for Mn^{3+} (d^4) and the spin-$\frac{3}{2}$ orbital singlet state $^4A_2\ [t_2^3]$ for Mn^{4+} (d^3), within 2^{nd} order perturbation theory the following Hamiltonian results (for details see Ref. [4]):

$$\begin{aligned}
\mathcal{H} &= \mathcal{H}_{\text{double-exchange}} + \mathcal{H}^{\text{2nd order}}_{\text{spin-orbital}} + \mathcal{H}_{\text{electron-JT}} + \mathcal{H}_{\text{electron-breathing}} + \mathcal{H}_{\text{phonon}} \\
&= \sum_{i,\delta,\alpha,\beta} (a_{i,\uparrow} a^\dagger_{i+\delta,\uparrow} + a_{i,\downarrow} a^\dagger_{i+\delta,\downarrow})\ t^\delta_{\alpha\beta}\ c^\dagger_{i,\alpha} n_{i,\bar{\alpha}} n_{i+\delta,\bar{\beta}} c_{i+\delta,\beta} \\
&\quad + \sum_{i,\delta,\kappa,\lambda} (J^\delta_{\kappa\lambda}\ \mathbf{S}_i \mathbf{S}_{i+\delta} + \Delta^\delta_{\kappa\lambda})\ P^\kappa_i P^\lambda_{i+\delta} \\
&\quad + g \sum_i \Big[(n_{i,\varepsilon} - n_{i,\theta})(b^\dagger_{i,\theta} + b_{i,\theta}) + (d^\dagger_{i,\theta} d_{i,\varepsilon} + d^\dagger_{i,\varepsilon} d_{i,\theta})(b^\dagger_{i,\varepsilon} + b_{i,\varepsilon}) \Big] \\
&\quad + \tilde{g} \sum_i (n_{i,\theta} + n_{i,\varepsilon} - 2 n_{i,\theta} n_{i,\varepsilon})(b^\dagger_{i,a_1} + b_{i,a_1}) \\
&\quad + \omega \sum_i \Big[b^\dagger_{i,\theta} b_{i,\theta} + b^\dagger_{i,\varepsilon} b_{i,\varepsilon} \Big] + \tilde{\omega} \sum_i b^\dagger_{i,a_1} b_{i,a_1}\,. \qquad (1)
\end{aligned}$$

The effective low-energy Hamiltonian $\mathcal{H}$ contains Schwinger bosons $a_{i,\mu}^{(\dagger)}$, i.e. $2\mathbf{S}_i = a_{i,\mu}^{\dagger}\boldsymbol{\sigma}_{\mu\nu}a_{i,\nu}$ ($\mu,\nu \in \{\uparrow,\downarrow\}$), fermionic holes $c_{i,\alpha}^{(\dagger)}$, phonons $b_{i,\alpha}^{(\dagger)}$ ($\alpha \in \{\theta,\epsilon\}$), and orbital projectors $P_i^{\kappa(\lambda)}$ ($\kappa,\lambda \in \{\xi,\eta,\zeta\}$). In Eq. (1), the first term, being proportional to t, corresponds to the well known double exchange interaction [5]. The second term appears to be a bit more involved, since a rather large number of accessible virtual excitations (proportional to t^2 and t_π^2) contribute (cf. Fig. 5). However, in all cases it is basically the product of a Heisenberg-type spin interaction and two orbital projectors. The coupling between the orbital degree of freedom of the e_g electrons and the optical phonon modes to lowest order in Q is modeled by the $E\otimes e$ Jahn-Teller Hamiltonian (third term) and a Holstein-type interaction (fourth term). The energy of the dispersionless optical phonons are given within harmonic approximation (fifth term). Using a density matrix based optimization procedure [6], we are able to retain the full quantum dynamic of these phonon modes within our numerical solution of the model on small clusters.

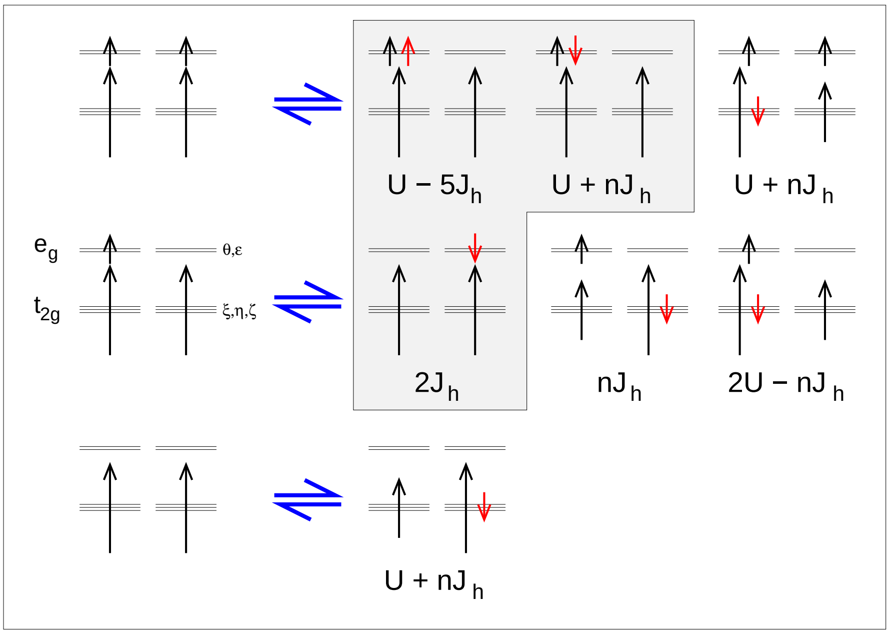

Fig. 5. Virtual excitations accounted for within 2$^{\text{nd}}$ order perturbation theory. The shaded region corresponds to t^2-terms, the other terms are proportional to t_π^2.

3 Numerical results

3.1 Undoped case

Undoped manganites ($LaMnO_3$, $PrMnO_3$) usually exhibit A-type anti-ferromagnetic order and strong Jahn-Teller distortion of the ideal perovskite structure. The origin of the observed magnetic order has been subject to discussions. While different band structure calculations [7] emphasize the importance of lattice distortions for the stability of anti-ferromagnetism, Feiner and Oleś [8] favoured a purely electronic mechanism.

Our calculation points out that both parameters, U/J_h and g, can drive a ferromagnetic to antiferromagnetic transition. The lower right panel of Fig. 6 shows the phase diagram of the purely electronic model, i.e., $g = 0$. We assumed $t = 0.4$ eV and $t/t_\pi = 3$ for the hopping integrals and characterized the magnetic phases according to the total spin of the ground state of the four site cluster. Starting from the "ferromagnetic" phase both, increasing U or g change the magnetic order of the ground state to "antiferromagnetism" (upper panels). In order to identify the corresponding orbital order we consider the local expectation value $\langle n_\theta - n_\varepsilon \rangle$. In view of the distinct driving

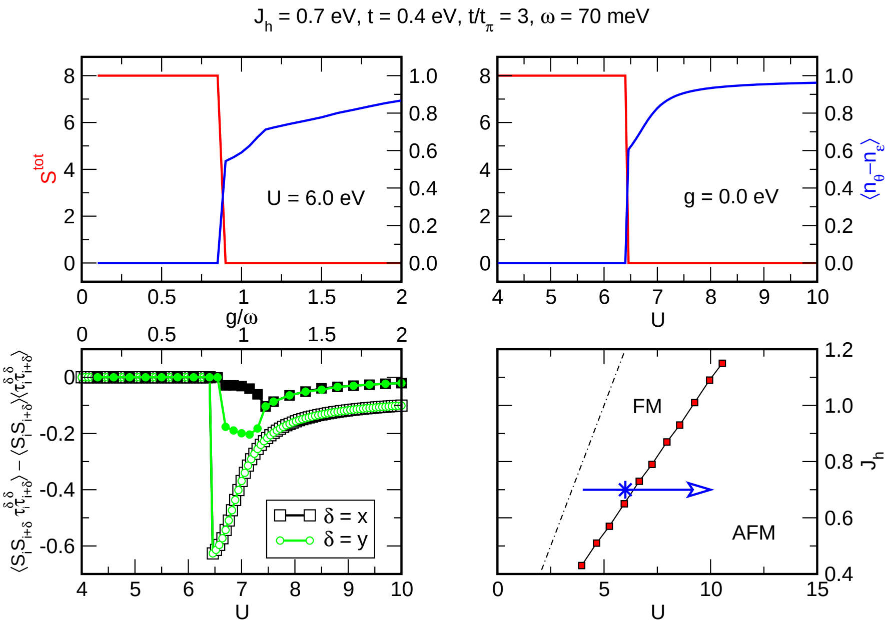

Fig. 6. Upper panels: Total spin S^{tot} (red line) and orbital order (blue line) of the ground state at variable electron-phonon coupling g and Coulomb interaction U. Lower left panel: Dependence of the spin-orbital correlations on electron-phonon ($U = 6$; filled symbols) and Coulomb ($g = 0$; open symbols) interactions. Lower right panel: phase diagram of the electronic model without phonons.

interactions both transitions appear to be very similar. However, we observe a significant difference, if we study the (de)coupling of spin and orbital degrees of freedom. The latter has been a rather controversial issue [9] in the case of the Kugel-Khomskii model [10], which contains the same kind of second order interactions, as our Hamiltonian, $\mathbf{S}_i\mathbf{S}_j\,\tau_i^\delta\tau_j^\delta$ (here the pseudo-spin operators τ_i^δ operate on the orbital degree of freedom). The lower left-hand panel indicates that the correlation $\langle\mathbf{S}_i\mathbf{S}_{i+\delta}\,\tau_i^\delta\tau_{i+\delta}^\delta\rangle - \langle\mathbf{S}_i\mathbf{S}_{i+\delta}\rangle\langle\tau_i^\delta\tau_{i+\delta}^\delta\rangle$ is a factor of $3-5$ smaller, if phonons are responsible for the FM to AFM transition. This behaviour is of course crucial for effective theories that are based on such decoupling schemes.

The change of orbital and phonon correlations is illustrated graphically in Fig. 7. Note however, that this is a rather suggestive picture. Studying the eigenstates of the orbital density matrix on a bond $\langle ij\rangle$, we can classify the states according to their behaviour under site exchange. Anti-symmetric states $|a\rangle_{ij} = \frac{1}{\sqrt{2}}\,(|\theta\rangle_i\otimes|\varepsilon\rangle_j - |\varepsilon\rangle_i\otimes|\theta\rangle_j)$ are unique, whereas symmetric states $|s(\varphi,\psi)\rangle_{ij} = \frac{1}{\|\cdot\|}\,(|\varphi\rangle_i\otimes|\psi\rangle_j + |\psi\rangle_i\otimes|\varphi\rangle_j)$ can be written as a product of two rotated orbitals $|\varphi\rangle_i = \cos(\varphi)|\theta\rangle_i + \sin(\varphi)|\varepsilon\rangle_i$ [4]. Since for small g the orbital configuration is antisymmetric for each bond, we can not draw the correct pattern, but choose only an artificial sketch of it.

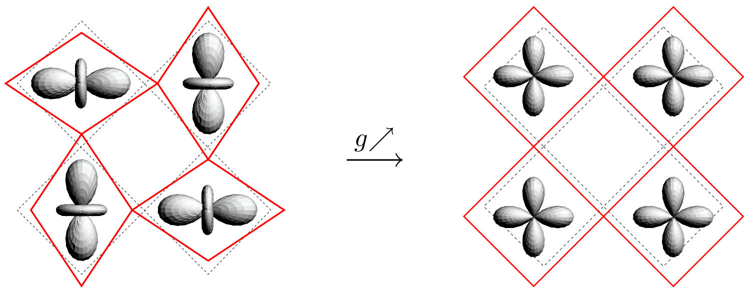

Fig. 7. Evolution of lattice and orbital correlations with increasing electron-phonon coupling g at doping $x = 0$ (schematic view).

3.2 Finite doping

As can be seen from the phase diagram of $La_{1-x}Sr_xMnO_3$ (Fig. 1), in the CMR regime ($0.15 < x < 0.5$), the metallic low-temperature phase is related to ferromagnetic long-range order stabilized by the double exchange interaction. Our numerical calculations for the weakly doped case ($x = \frac{1}{4}$) corroborate the enhancement of ferromagnetic correlations. However, if strong electron-phonon coupling causes localization of the carriers the spin order switches to antiferromagnetism. This coincidence is illustrated in Fig. 8 (upper panels) showing the total spin of the cluster and the kinetic energy in

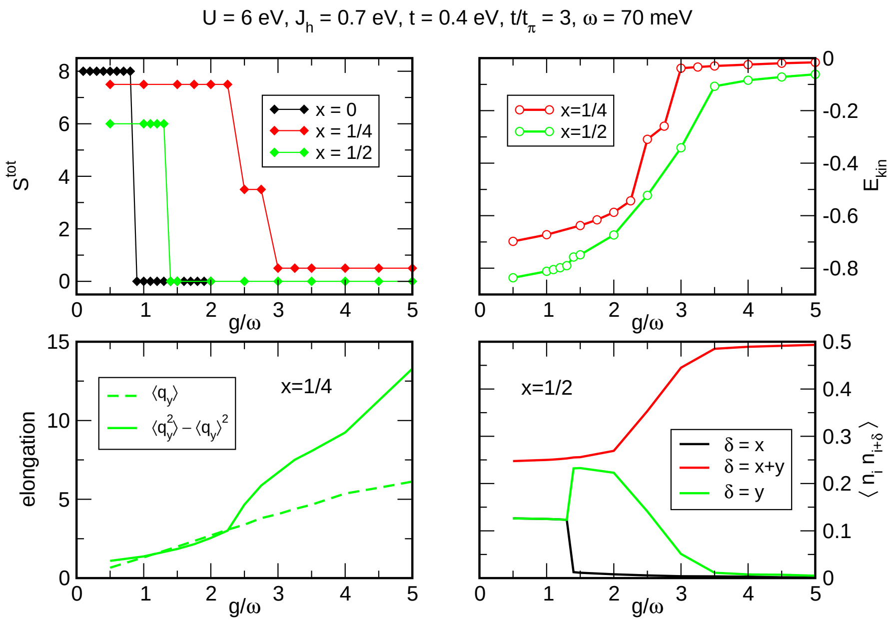

Fig. 8. Upper panels: Total spin S^{tot} and kinetic energy E_{kin} as a function of electron-phonon coupling strength g/ω at various doping levels x. Lower panel: Expectation values $\langle q_y \rangle$ and $\langle q_y^2 \rangle - \langle q_y \rangle^2$ of the bond length in y direction at $x = 1/4$ (left) and density-density correlations at $x = 1/2$.

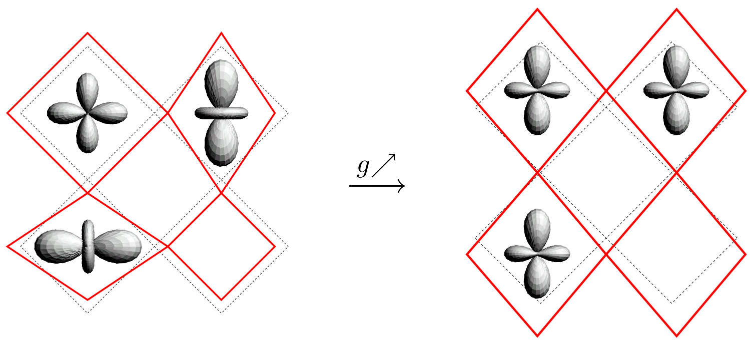

Fig. 9. Evolution of lattice and orbital correlations with increasing electron-phonon coupling g at doping $x = 1/4$.

the ground state. The change in the magnetic order is accompanied by the appearance of a lattice distortion and a signature in the fluctuation of the bond length ($\propto \langle q_{x/y}^2 \rangle - \langle q_{x/y} \rangle^2$), which reminds of the data measured close to the critical temperature by Booth et al. [11] (lower left panel). The orbital orientation at the sites which surround the hole is sketched in Fig. 9. Obviously increasing g isolates the lattice sites, each optimizing electron-phonon interaction individually and uncorrelated with the neighbours.

At doping $x = \frac{1}{2}$ the picture is more involved. Strong Coulomb and electron-phonon interactions tend to order the charges in diagonal direction, i.e., in an AB-structure (compare Fig. 8, lower right panel). This allows for a rather large anti-ferromagnetic spin exchange $\propto t^2/J_h$. Consequently ferromagnetic order is unstable at much lower values of g. The ferromagnetic to antiferromagnetic transition is not connected to charge localization and causes only a tiny jump of the kinetic energy. Considering the most relevant eigenstate of the bond orbital density matrix, we observe a symmetric order of complex orbitals along the diagonal [4]. After charge localization is achieved at large g, neighbouring sites are again uncorrelated with respect to orbital ordering and are in some real mixed-orbital state.

4 Performance analysis on supercomputers

Exact diagonalization studies of microscopic electron-phonon models involve very large sparse matrices, even for small clusters. Since the matrix size accessible for diagonalization determines the quality of our results, both continuous access to the most powerful supercomputers and steady improvements of algorithms and implementations are the technical basics of our project. Over the last years Lanczos, Jacobi-Davidson, density-matrix, kernel-polynomial expansion, and maximum-entropy algorithms have been successfully implemented on numerous architectures including CRAY T3E, NEC SX-4/5, IBM SP, Fujitsu VPP700 and Hitachi SR8000 supercomputers. The numerical core of these algorithms is a matrix-vector multiplication (MVM), involving mega-dimensional matrices. Although the matrices are extremely sparse ($\approx 10-50$ non-zero entries per row) a memory saving, parallel MVM implementation has been developed, where the non-zero matrix entries are recomputed in each MVM step. The parallel MVM is implemented in FORTRAN and uses the `MPI` library for data exchange between processors. For CRAY T3E systems `MPI` calls have been replaced by calls to CRAY `shmem` library in selected performance critical routines. With a total memory requirement of approximately four vectors of matrix-dimension we are able to perform exact diagonalization studies up to matrices dimensions of 30 billion on present-day german supercomputers.

To demonstrate the scalability of our implementation we consider the more simplified Holstein Hubbard Hamiltonian

$$H = -t\sum_{i,\sigma}(c^{\dagger}_{i\sigma}c_{i+1\sigma} + \text{H.c.}) + U\sum_{i} n_{i\uparrow}n_{i\downarrow} + g\omega_0\sum_{i,\sigma}(b^{\dagger}_{i} + b_{i})n_{i\sigma} + \omega_0\sum_{i} b^{\dagger}_{i}b_{i}, \tag{2}$$

which, nevertheless, can be taken as a generic model for the interaction of electron and lattice degrees of freedom in solids. Here $c^{\dagger}_{i\sigma}$ creates a spin-σ electron at Wannier site i ($n_{i,\sigma} = c^{\dagger}_{i\sigma}c_{i\sigma}$), $b^{\dagger}_{i}$ creates a local phonon of frequency

ω, t denotes the hopping integral, U is the on-site Hubbard repulsion, g is a measure of the electron-phonon coupling strength. The Holstein Hubbard Hamiltonian allows a scaling of the corresponding matrix size by increasing the number of electrons without changing the principle matrix structure. Since available memory is the limiting factor in our calculations we have fixed a matrix dimension of 2 million per processor in the scalability study presented in Fig. 10. It is well known that the single processor performance of

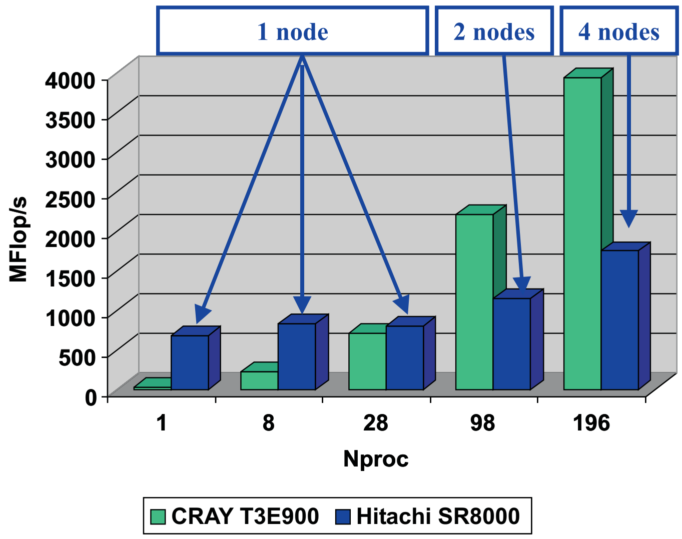

Fig. 10. Scaling study with fixed matrix size of 2 million per CRAY T3E processor. The total performance is depicted as a function of CRAY T3E processors (`Nproc`) used in the calculations. For comparison the corresponding performance numbers of the Hitachi SR8000-F1 at LRZ Munich using one (`Nproc=1,8,28`), two (`Nproc=98`) and four (`Nproc=196`) nodes are given.

sparse MVM algorithms is bounded by the quality of the memory access and thus a performance of roughly 33 MFlop/s has been measured on one processor. For the parallel runs, however, our implementation benefits from the high scalability of CRAY T3E systems and we find a parallel speed-up of approximately 130 on 196 processors, even for complex communication patterns as used in the benchmarks. Nonetheless about 30 (60) CRAY T3E processors are required to get the same performance (amount of memory) as one Hitachi SR8000-F1 node at LRZ Munich using a hybrid parallel programming approach.

The leading edge simulations had to be done on the LRZ system because of the larger main memory which is not available at the HLRS at present.

However, even the size of the memory in Munich will not be enough for the problems that we intend to solve in near future. Therefore the installation of a more powerful system with a large aggregate amount of memory at the HLRS would be highly desirable.

5 Concluding Remarks

The work presented in this report is an example for the reliability and predictive power of many-body calculations performed on modern supercomputers. The implementation of the various optimized program packages on the CRAY T3E at the HLRS Stuttgart provided new and exciting insights into the complex interplay of charge, spin, orbital and lattice degrees of freedom in the currently most intensive studied novel materials: the quasi-1D metals, spin chains and charge-density-wave systems, high-T_c cuprates, polaronic nickelates and colossal magneto-resistance manganites. For doped CMR manganites we showed explicitely how the electron-phonon interaction effectively controls spin and orbital order by affecting charge mobility and orbital degrees of freedom. Our exact diagonalization study of even a small system provides detailed information about correlations and driving interactions behind the rich phase diagram of the manganites. This may support the development of approximate theories.

Acknowledgements

We are indebted to the to the HLR Stuttgart, NIC Jülich, LRZ München and NIC Jülich for the generous granting of their parallel computer facilities. This work was supported by the Deutsche Forschungsgemeinschaft under project Fe 398-1/2.

References

1. S. Jin, T. H. Tiefel, M. McCormack, R. A. Fastnach, R. Ramesh, and L. H. Chen, Science **264**, 413 (1994).
2. Y. Tokura and Y. Tomioka, J. Magn. Magn. Mater. **200**, 1 (1999); J. M. D. Coey, M. Viret, and S. von Molnar, Adv. Phys. **48**, 167 (1999); E. Dagotto, T. Hotta, and A. Moreo, Physics Reports **344**, 1 (2001).
3. J. Hemberger *et al.*, arXiv:cond-mat/0204269; M. Paraskevopoulos *et al.*, J. Phys.: Condens. Matter **12**, 3993 (2000); J. Magn. Magn. Mater. **211**, 118 (2000).
4. A. Weiße and H. Fehske, in preparation.
5. C. Zener, Phys. Rev. **82**, 403 (1951); P. W. Anderson and H. Hasegawa, Phys. Rev. **100**, 675 (1955); K. Kubo and N. Ohata, J. Phys. Soc. Jpn. **33**, 21 (1972); A. Weiße, J. Loos, and H. Fehske, Phys. Rev. B **64**, 054406 (2001).

6. A. Weiße, H. Fehske, G. Wellein, and A. R. Bishop, Phys. Rev. B **62**, R747 (2000); A. Weiße, G. Wellein, and H. Fehske, *High Performance Computing in Science and Engineering '01* edited by E. Krause and W. Jäger, Springer-Verlag, Heidelberg (2002), pp 131-144.
7. D. D. Sarma *et al.*, Phys. Rev. Lett. **75**, 1126 (1995); W. E. Pickett and D. J. Singh, Phys. Rev. B **53**, 1146 (1996); S. Satpathy, Z. S. Popović, and F. R. Vukajlović, Phys. Rev. Lett. **76**, 960 (1996); I. Solovyev, N. Hamada, and K. Terakura, Phys. Rev. Lett. **76**, 4825 (1996).
8. L. F. Feiner and A. M. Oleś, Phys. Rev. B **59**, 3295 (1999).
9. G. Khaliullin and V. Oudovenko, Phys. Rev. B **56**, R14243 (1997); L. F. Feiner, A. M. Oleś, and J. Zaanen, J. Phys. Condens. Matter **10**, L555 (1998).
10. K. I. Kugel and D. I. Khomskii, Sov. Phys. JETP **37**, 725 (1973).
11. C. H. Booth *et al.*, Phys. Rev. Lett. **80**, 853 (1998).